ADVANCED OPTICAL MATERIALS
www.advopticalmat.de

Symmetry-Determined Lasing from Incommensurate Moiré Nanoparticle Lattices

*Fabio M. Fasanelli, Francisco Freire-Fernández, and Teri W. Odom**

This paper describes how moiré plasmonic nanoparticle lattices can exhibit lasing action over a broad wavelength and wavevector range. Moiré nanolithography is combined with the PEEL (Photolithography, Etching, Electron-beam deposition, and Lift-off) process to fabricate in-plane incommensurate lattices with optical properties beyond the restricted geometries of Bravais lattices. Because of increased rotational symmetry, moiré lattices support a larger number of transverse electric and transverse magnetic modes relative to their periodic base lattices. It is found that multidirectional lasing characteristics can be predicted by the symmetry of the moiré reciprocal lattice. Incommensurate moiré plasmonic lattices combine advantages of the dense band structures observed in aperiodic lattices with that of predicted modes in Bravais lattices for light-based technologies in coherent light sources and multiplexed data transfer.

1. Introduction

Since the demonstration of magic-angle superconductivity in twisted bilayer graphene,[1] moiré phenomena have been observed in 2D electronic materials, including light-induced ferromagnetism,[2] topological edge states,[3,4] and Mott insulation.[5] Because these superlattices are constructed by superimposing two or more layers of a base lattice at an angular offset,[6] the properties of electronic moiré materials are limited by their fixed atomic lattice structure and relative stacking orientation. The twist angle determines whether a moiré pattern is defined as commensurate (periodic superlattice) or incommensurate (aperiodic superlattice with at least two periodicities whose ratio is irrational).[7] The exotic phenomena found in electronic moiré systems have motivated the study of photonic analogs, including stacked lattices that have shown circular dichroism and ultralong-range coupling[8,9] and in-plane photonic lattices that have exhibited plasmonic bandgaps and lasing from flat bands.[10–12] In contrast to electronic materials, photonic moiré lattices can be constructed from arbitrary base lattices with respect to both symmetry and pitch in a single layer.

Plasmonic nanoparticle (NP) lattices are a promising platform for designing in-plane moiré lattices because they support surface lattice resonances (SLRs), hybrid modes from coupling between the diffractive modes of the lattice and localized surface plasmons of the NPs.[13] The large scattering cross-sections and ultra-confined electric-field enhancement of periodic plasmonic materials offer advantages over dielectric photonic materials.[14] High-quality SLR modes with narrow resonances require at least 30 periods,[13,15,16] and large-scale patterns have shown ultra-narrow linewidths (<2 nm) at visible[17] and near-infrared wavelengths.[18,19] Since incommensurate moiré lattices lack a unit cell, determining a minimum array size for optimal moiré SLR modes requires an approximation; for commensurate lattices, moiré periodicities can be orders of magnitude larger than the base lattice (10–100s of microns).[20,21] Incommensurate moiré patterns larger than ≈mm^2 are therefore desirable for plasmonic lattices with properties in the visible regime.

When combined with gain materials,[22–25] plasmonic Bravais lattices can function as distributed feedback cavities whose lasing emission characteristics are usually from band crossings at high-symmetry points (Γ, X, M, and K).[26–29] Bravais lattices have also facilitated two-color lasing by exploiting low-symmetry patterns on a single substrate,[22,30] although three-color lasing has required multiple periodic lattices.[31,32] Since aperiodic lattices support broadband optical responses, multi-modal lasing from a single structure is possible within the emitter bandwidth.[33] Other metasurfaces with dense photonic band structures, including superlattices and waveguided gratings, have also shown multi-modal emission.[33–39] In general, there are challenges in predicting the energies and directions of lasing action from more complex, non-Bravais cavities. For periodic superlattices, the size and spatial distribution of NPs within the unit cell can

F. M. Fasanelli, F. Freire-Fernández, T. W. Odom
Department of Chemistry
Northwestern University
Evanston, IL 60208, USA
E-mail: todom@northwestern.edu

T. W. Odom
Department of Materials Science and Engineering
Northwestern University
Evanston, IL 60208, USA

The ORCID identification number(s) for the author(s) of this article can be found under https://doi.org/10.1002/adom.202400797

DOI: 10.1002/adom.202400797

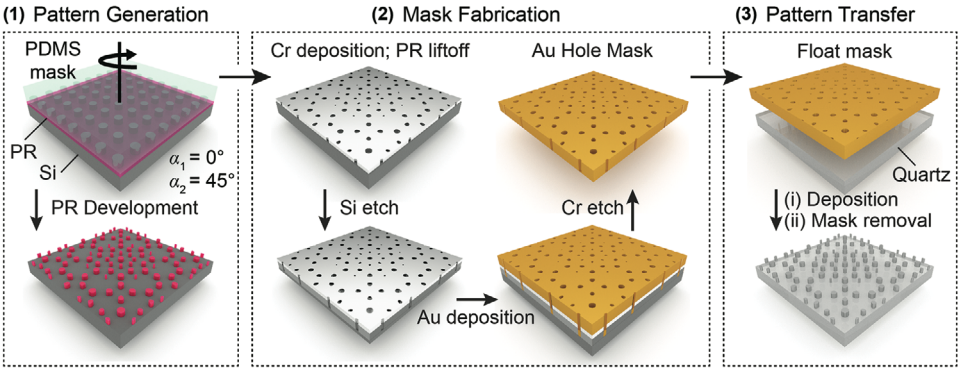

Scheme 1. Combination of moiré nanolithography with the PEEL process.

influence lasing from some modes, but selective lasing from specific modes has not been demonstrated.[34,39]

Here we show how incommensurate moiré lattices support lasing characteristics with specific wavelengths and directions determined by the symmetry of the reciprocal lattice. We fabricated large-area, eightfold rotationally symmetric moiré aluminum NP lattices by incorporating moiré nanolithography[6] into the PEEL process. The moiré lattice supported more transverse electric and transverse magnetic modes than the fourfold, square base lattice over the same visible wavelength range. Angle-resolved photoluminescence measurements revealed lasing at multiple angles with similar thresholds. Since the incommensurate moiré lattice has a dense optical band structure, we could achieve lasing at four different colors (green, orange, red, and near-infrared) from the same substrate depending on the gain bandwidth of the different organic dye solutions. This work shows how lasing from complex band structures can be controlled via the rotational symmetry of the lattice cavity.

2. Results and Discussion

Scheme 1 summarizes the key three steps to fabricate plasmonic NP moiré lattices. In step 1 (*pattern generation*), moiré nanolithography[6] is used for large-area patterning of subwavelength features in photoresist. In brief, a thin layer of positive-tone photoresist on a Si wafer is subjected to multiple exposures of UV light through a transparent, elastomeric phase-shifting mask patterned with a single base lattice. According to the design rules,[6] the number of exposures for an *n*-fold rotationally symmetric lattice is *n* divided by the rotational symmetry of the base lattice; the offset angle α between exposures is $\frac{360°}{n}$. To fabricate an eightfold incommensurate moiré pattern, we carried out two exposures (α_1 = 0° and α_2 = 45°) through a poly(dimethylsiloxane) (PDMS) mask patterned with a square lattice (a_0 = 500 nm) of air cylinders. After development, the moiré pattern is revealed. Although electron-beam lithography can readily create patterns over hundreds of microns,[40,41] there are challenges, including proximity effects, for scaling to cm^2 areas.

In step 2 (*mask fabrication*), we used the PEEL (Photolithography, Etching, Electron-beam deposition, and Lift-off) process[42] to transfer the moiré patterns in photoresist into a free-standing Au hole array mask. PEEL is a well-known pattern transfer technique to fabricate plasmonic NP lattices but had not been combined with moiré nanolithography. First, Cr was deposited and lifted off to create a Cr mask for dry etching the underlying Si wafer. Then, Au (100 nm) was deposited, and the Cr layer was wet-etched to release the Au mask from the substrate. In step 3 (*pattern transfer*), the Au mask was placed on a quartz substrate, and aluminum (Al) (50 nm) was deposited. The Au moiré mask was removed with cellophane tape, resulting in an eightfold incommensurate moiré pattern of plasmonic Al NPs.

Figure 1a represents a scanning electron microscopy (SEM) image of an Al NP lattice with eightfold rotational symmetry. As expected, the reciprocal lattice calculated by the fast Fourier transform is also eightfold (Figure 1b). A ±0.2° error in the offset

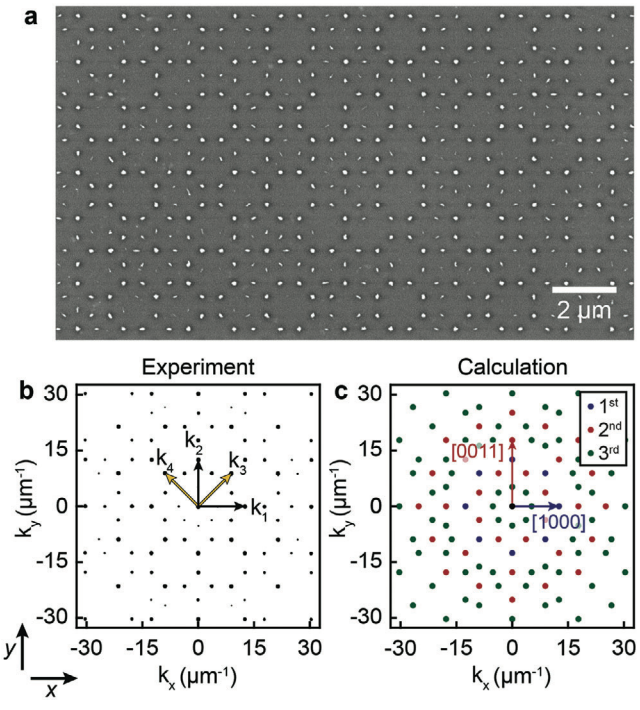

Figure 1. Moiré lattice of Al NPs with eightfold rotational symmetry. a) SEM image of as-fabricated Al NPs in an eightfold lattice constructed from a 500-nm square base lattice. b) Experimental reciprocal lattice calculated from (a). c) Calculated reciprocal lattice including up to third-order points.

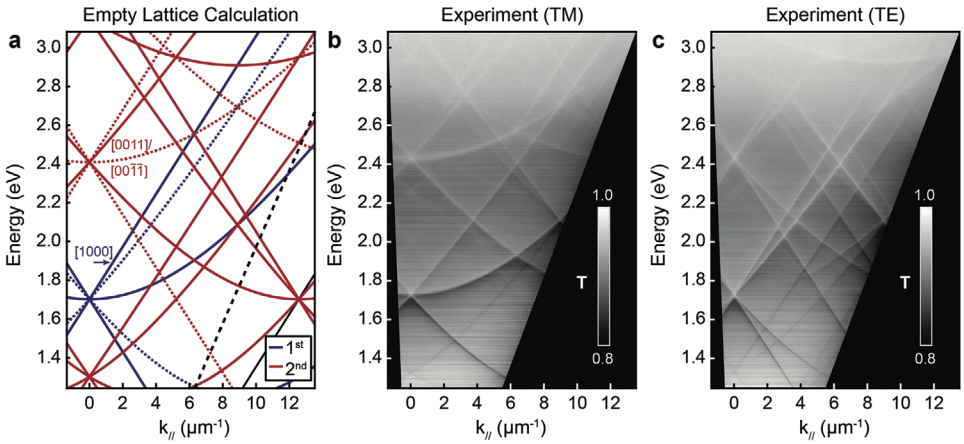

Figure 2. Linear optical dispersion is well-described by the empty lattice approximation. a) Calculated dispersion of an empty eightfold lattice. Dashed modes originate from the second sublattice. The light line is black and dashed. Measurements of energy- and wavevector-resolved optical transmission under b) TM-polarization and c) TE-polarization.

angle of the lattice was determined by calculating the difference in angle between experimental lattice vectors. In both the real-space and reciprocal-space lattices, not all of the features have the same size or intensity because of a drawback in moiré nanolithography, where there is a range of particle sizes and shapes even as the symmetry of the lattice remains robust.[6] The non-uniformity is because of the incomplete overlap of the nanopatterns in the PDMS from the different exposures; the calculations confirm (Figure S1a, Supporting Information). The experimental reciprocal lattice closely matched calculations carried out using four lattice vectors separated in angle by 45° (Figure 1c). Each of the lattice vectors of the incommensurate moiré lattice can be indexed by the sublattice vectors, where $[k_1 k_2]$ (black) and $[k_3 k_4]$ (yellow) are from the first and second sublattices, respectively. Indexing the moiré modes with the four vectors as $[k_1 k_2 k_3 k_4]$ enables the order of a given mode to be calculated by summing the absolute values of the lattice vectors, similar to periodic lattices.[10] Figure S1b (Supporting Information) displays higher order modes (≥3) supported by the lattice. Unlike commensurate moiré lattices, incommensurate lattices do not have a defined Brillouin zone, and the first-order modes in Figure 1c are not the lowest-energy modes from the eightfold symmetric lattice.

Although incommensurate moiré lattices are aperiodic, a commensurate approximation can be made using Pythagorean triples[20] that result in large unit cells. For modeling the optical properties of plasmonic lattices, finite-difference time-domain (FDTD) calculations are generally preferred; Figure S2 (Supporting Information) shows simulations of the transmission and near fields of an eightfold lattice. However, these simulations are computationally expensive for micron-sized, many-particle unit cells at off-normal angles of incidence. Since SLR modes form from the coupling of localized surface plasmons of NPs to diffraction modes of the lattice, we can use the empty lattice approximation to estimate the mode energies. Diffraction modes of an empty lattice must satisfy:

$$\left|\boldsymbol{k}_{//} + \sum \boldsymbol{G}_i\right| = \left|\boldsymbol{k}_{inc}\right| \quad (1)$$

where $\boldsymbol{k}_{//} = \boldsymbol{k}_x + \boldsymbol{k}_y$ is the in-plane wavevector of the incident light, $\boldsymbol{G}_i$ is the grating vector of sublattice i, and $\boldsymbol{k}_{inc} = \frac{nE}{\hbar c}$ is the wavenumber of an incident photon with energy E traveling in a medium with refractive index n. Note: we consider sublattices only in reciprocal space and distinguish them from the base lattice in real space that is used to generate the moiré pattern. **Figure** 2a shows the calculated bands from Equation (1) through second-order modes; modes up to fifth order are displayed in Figure S3 (Supporting Information). We aligned the lattice vectors $\boldsymbol{k}_1$ and $\boldsymbol{k}_2$ along the x-axis and y-axis for consistency. Hence, the first sublattice is a square lattice oriented along the Γ-X direction, while the second sublattice is a square lattice oriented at a 45° offset angle, along the Γ-M direction. The linear dispersion modes are transverse electric (TE), and the parabolic dispersion modes are transverse magnetic (TM).

The experimental dispersion diagrams under TM and TE polarization (Figure 2b,c) closely follow calculations in Figure 2a, which highlights the strong diffractive character of the moiré SLR modes. Since the [±10] and [0 ± 1] modes in the first sublattice are TE and TM modes (Figure S4, Supporting Information), respectively, the equivalent [±1000] and [0 ± 100] modes in the eightfold moiré lattice are TE and TM modes. However, the [00 ± 10] and [000 ± 1] modes are hybrid modes analogous to the [±10] and [0 ± 1] modes of a square lattice along the Γ-M direction since they originate from the second sublattice. Thus, moiré modes associated with sublattice modes retain their polarization response from that sublattice.

The combination of modes of the two sublattices in the moiré lattice results in a higher number of TE and TM modes in the same wavelength range. For example, the [±1±1] set of modes in the first sublattice contains only hybrid modes (Figure S4, Supporting Information). Since the [±1±1] set of modes in the second sublattice contains TE and TM modes, the set of second-order modes in the moiré lattice at 2.4 eV (includes [0011] / [00-1-1]) also has TE and TM character. This effect occurs because the Γ-X and Γ-M directions of the fourfold base lattice are offset by the same angle as the fourfold sublattices of the eightfold moiré lattice. Furthermore, combining the lattice vectors of the

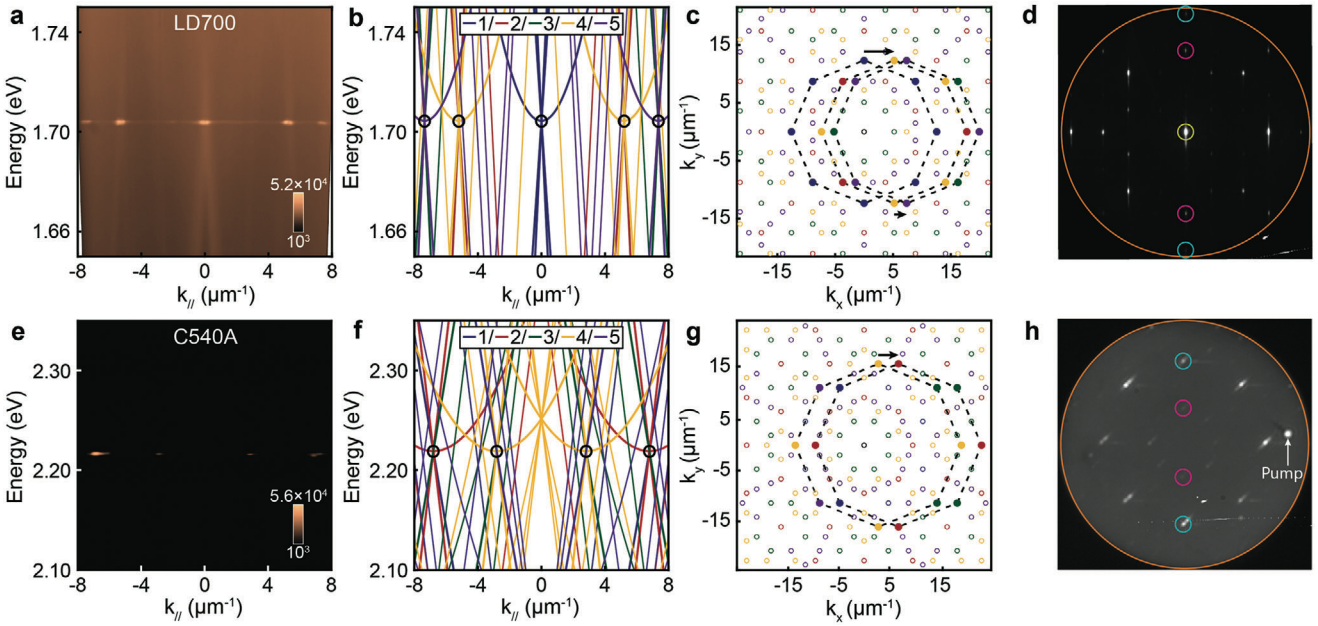

Figure 3. Symmetric crossings support concurrent lasing emission. a) Energy- and wavevector-resolved PL measurements above the lasing threshold for 17 mM LD700 dye in DMSO. b) Calculated diffraction modes. The legend indicates the order of the modes, and the black circles indicate the crossings associated with lasing. c) Symmetry of lasing modes for LD700. d) Back focal plane image of emission above threshold. The orange ring denotes a numerical aperture of 0.95, which corresponds to an angle of 72°. e) Energy- and wavevector-resolved PL measurements above the lasing threshold for 40 mM C540A dye in DMSO with the sample twisted 22.5° about the surface normal. f) Calculated diffraction modes. g) Symmetry of lasing modes for C540A. h) Back focal plane image of emission above the threshold.

two sublattices creates TE or TM modes only accessible in the moiré structure. For instance, the [-101-1] mode ($\boldsymbol{k}_{//} = 4\ \mu m^{-1}$, $E = 1.25$ eV) is derived from three lattice vectors and is TE-polarized (Figure 2c; Figure S3, Supporting Information).

Although the first- and second-order modes in Figure 2a do not account for all the measured modes, calculations up to the fifth order can (Figure S3b, Supporting Information). Some of the higher-order modes, however, are not observed in the white-light transmission measurements. For example, a crossing between three third-order and five fifth-order modes ($\boldsymbol{k}_{//} = 7.3\ \mu m^{-1}$, $E = 1.7$ eV) is expected, but measurements only showed a third-order mode ([-110-1]) (Figure 2b,c). To observe more high-order moiré modes, we combined the NP lattice with an organic dye LD700 solution and measured the photoluminescence (PL). Because of Purcell effects, dye molecules can be used to reveal bands based on their emission properties (Figure S5, Supporting Information) as well as result in lasing action from SLR cavity modes.[28,29]

Using a Fourier microscopy setup (Experimental Section), we observed multidirectional lasing with narrow linewidths (<1 nm; Figure S6, Supporting Information) at a single energy after pumping the system with a 1-kHz, 100-fs-pulsed laser (665 nm). By comparing the measured and calculated band structures above the threshold (**Figure 3**a,b), we determined that the off-normal lasing emission (measured at ±37° and ±58°) is from crossings between second- and fourth-order modes (red and yellow) and crossings between third- and fifth-order modes (green and purple), respectively (**Table 1**). The pair of lasing spots from the crossings of second- and fourth-order modes have the same threshold (27 μJ cm^{-2}) as the emission from the Γ point at $\boldsymbol{k}_{//} = 0$; the pair of lasing spots from the crossings between third- and fifth-order modes have thresholds ≈3% higher (Figure S7, Supporting Information). These nearly identical thresholds are unexpected because scattering and absorption cross-sections typically decrease with increased mode order. We note that crossings at nearby energies share modes with similar quality factors as the crossings associated with lasing. Since no lasing was observed at any other energies, however, we conclude that the quality factor alone cannot explain these observations.

These mode crossings can be related to the symmetry of the moiré band structure. Each set of modes associated with lasing forms congruent octagons in the reciprocal lattice that are translated from the Γ point (Figure 3c, positive k_x-direction). Identical sets of these congruent octagons exist along both positive and negative directions of each lattice vector in an eightfold

Table 1. Modes associated with lasing from the LD700 dye.

$k_{//}$ [μm^{-1}]	−7.3	−5.2	0	5.2	7.3
Intersecting Modes	[20-12] / [20-21], [21-11] / [2-1-11], [2001] / [20-10], [30-11], [10-11]	[-1010] / [-100-1], [-111-1] / [-1-11-1], [-102-1] / [-101-2], [001-1], [-201-1]	[000-1] / [0010], [0-100] / [0100], [00-10] / [0001], [-1000], [1000]	[10-10] / [1001], [1-1-11] / [11-11], [10-21] / [10-12], [00-11], [20-11]	[-201-2] / [-202-1], [-2-11-1] / [-211-1], [-200-1] / [-2010], [-301-1], [-101-1],

Table 2. Modes associated with lasing from the C540A dye.

$k_{//}$ [μm^{-1}]	−6.8	−2.9	2.9	6.8
Intersecting Modes	[0001] / [0-100], [1-100] / [0011], [1011] / [1-110], [1010], [0-101]	[-12-1-1] / [-11-1-2], [01-1-2] / [-120-1], [020-1] / [010-2], [020-2], [-11-1-1]	[1-211] / [1-112], [0-112] / [1-201], [0-201] / [0-102], [0-202], [1-111]	[000-1] / [0100], [-1100] / [00-1-1], [-10-1-1] / [-11-10], [-10-10], [010-1]

symmetric pattern; there are 17 octagons total, including the one centered at the Γ point. The lasing spots circled in the back focal plane image in Figure 3d correspond to the angle-resolved emission measurement in Figure 3a and map to the pattern of octagons in Figure 3c. The wavevectors from the center of each octagon are the same as the directions of the associated lasing beams in Figure 3a–d.

In addition to lasing from the Γ point ($\boldsymbol{k}_{//} = 0$), there are two concentric rings of lasing spots in Figure 3d; each ring represents a single magnitude of $\boldsymbol{k}_{//}$ and thus a different angle from the surface normal. The spots in the inner ring (pink circles) correspond to octagons of second- and fourth-order modes (red and yellow vertices, Figure 3c), and the spots in the less intense, outer ring (cyan circles) correspond to octagons of third- and fifth-order modes (green and purple vertices, Figure 3c). Other faint spots in the back focal plane can be explained by symmetry as Purcell-enhanced emission (Figures S8 and S9, Supporting Information). For reference, the back focal plane image of lasing from a 500-nm square lattice (the base lattice of the eightfold moiré lattice in our experiments) only shows a single lasing spot at the Γ point (Figure S10, Supporting Information). The connection between lattice symmetry and lasing characteristics can be described using the light-cone model for the modes located at the vertices of the octagons (Figure S11, Supporting Information). At the isoenergetic plane of lasing, the cross-sections of eight light cones overlap at the center of each octagon to form standing waves that can support optical feedback.[26] Since emission was observed where the eight light cones (i.e., eight modes) cross, but not at locations where fewer modes intersect, we propose that mode degeneracy is a determining factor to achieve lasing action at different magnitudes of $\boldsymbol{k}_{//}$. However, although eight modes intersect at ($\boldsymbol{k}_{//} = \pm 6.3$ μm^{-1}, $E = 1.71$ eV), there was no associated lasing emission at this angle; analyzing in reciprocal space, we found irregular, eight-sided polygons that had only twofold rotational symmetry (Figure S12, Supporting Information). Therefore, we hypothesize that both high rotational symmetry and mode degeneracy are needed to realize multidirectional lasing from incommensurate moiré lattices.

To test this symmetry-lasing relationship, we probed another portion of the band structure with multiple crossings that similarly form congruent octagons in reciprocal space. Using C540A dye in DMSO for its desirable gain overlap with this region, we observed four lasing beams at the same energy with nearly identical thresholds from the expected crossings (Figure 3e,f). Because the associated octagons do not translate along the moiré lattice vectors but exactly at 22.5° between them, we rotated the moiré lattice in-plane 22.5° before optical characterization. The outer pair of crossings ($\boldsymbol{k}_{//} = \pm 6.8$ μm^{-1}) is formed by first-, second-, and third-order modes while the inner pair ($\boldsymbol{k}_{//} = \pm 2.9$ μm^{-1}) is formed by third-, fourth-, and fifth-order modes (**Table 2**).

In reciprocal space, these crossings form congruent octagons with sizes larger than those in Figure 3c because the lasing emission is at a higher energy (Figure 3g). Since the pair of octagons also forms an eightfold symmetric pattern via rotation at 45° intervals about the origin, we expected and observed 16 lasing beams in the back focal plane image (Figure 3h). The light-cone model indicates that eight overlapping cross-sections exist at the center of each octagon, which describes the directions of emission (Figure S11, Supporting Information), supporting our symmetry design principle. Other methods that can describe emissive non-Bravais lattice systems, such as the structure factor, cannot fully explain our observations.[33,39]

In addition, we evaluated whether the eightfold incommensurate moiré lattice could exhibit lasing action in energy ranges of the band structure that lacked high-symmetry crossings. We combined the moiré lattice with R6G in DMSO and, after pumping the system at 534 nm, off-normal lasing can still be observed but only at one absolute value of $\boldsymbol{k}_{//}$ (**Figure 4a**). The crossings associated with lasing ($\boldsymbol{k}_{//} = \pm 2.6$ μm^{-1}, $E = 2.1$ eV) are from one first-order ([1000], [-1000]) and one second-order ([00-11], [001-1]) mode (Figure 4b). Despite the presence of higher order, isoenergetic crossings at different $|\boldsymbol{k}_{//}|$ in the empty lattice approximation (Figure S13a, Supporting Information), additional lasing beams were not observed, likely because the crossings consist only of pairs of modes with low rotational symmetry (twofold) instead of the high symmetry (≥eightfold) on which we base our hypothesis.

To investigate lasing at NIR wavelengths, we excited LDS821 dye in DMSO on the eightfold moiré NP lattice at 534 nm (Figure 4d). These lasing beams originate from crossings between one third-order ([-101-1], [10-11]) and two fourth-order ([-210-1] / [-2-110], [2-101] / [21-10]) modes ($\boldsymbol{k}_{//} = \pm 5.9$ μm^{-1}, $E = 1.5$ eV) (Figure 4e). Although there are six additional isoenergetic crossings, each consisting of five, seven, or nine modes (Figure S13d–g, Supporting Information), lasing was not observed at the tested pump fluences. In the light-cone model, there are more overlaps for these crossings than those associated with lasing. However, the crossings not only have different degeneracies but also form rotationally asymmetric polygons in reciprocal space, which is consistent with our hypothesis that both mode degeneracy and symmetry are important.

3. Conclusion

In summary, we demonstrated that reciprocal lattice symmetry can determine the energy and direction of lasing emission from incommensurate moiré lattices. Rotational symmetry can now be considered as a design principle to predict the characteristics of multidirectional lasing beams with the same wavelength. We expect that our results are general regarding base lattice

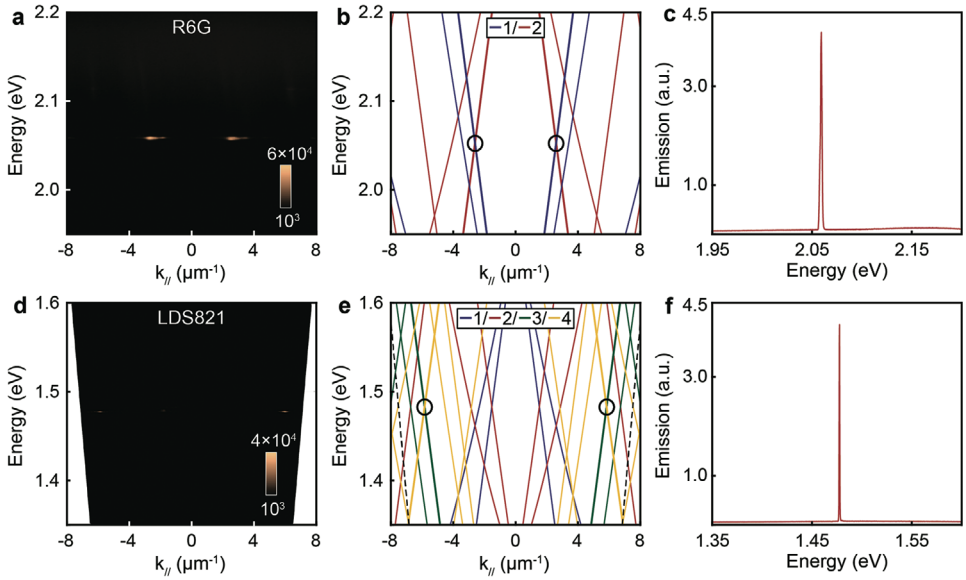

Figure 4. Incommensurate lattices support lasing across a broad energy range. a) Energy- and angle-resolved PL measurements above the lasing threshold for 16.7 mM R6G dye in DMSO. b) Calculated diffraction modes. c) Single-wavevector slice of the lasing emission from R6G at 2.6 μm^{-1}. d) Energy- and angle-resolved PL measurements above the lasing threshold for 5.0 mM LDS821 dye in DMSO. Calculated diffraction modes. f) Single-wavevector slice of the lasing emission from LDS821 at 5.9 μm^{-1}.

periodicity and rotational symmetry. For example, decreasing the periodicity of the base lattice from 500 to 400 nm would shift the symmetry-determined lasing to higher energies given appropriate gain. Also, higher-order rotational symmetries should exhibit analogous phenomena with different beam multiplicity; twelvefold symmetry lattices, for example, are expected to produce off-normal beams in multiples of 12. Moreover, our scalable nanofabrication method can generate incommensurate moiré lattices from base lattices with symmetries not possible for electronic materials (e.g., fourfold, rectangular), which opens prospects for moiré materials with unusual geometries and properties.

4. Experimental Section

Fabrication of Incommensurate Moiré Al NP Lattices: Moiré nanolithography[6] was used to fabricate an eightfold incommensurate pattern of S1805 G2 photoresist (PR) posts on a Si (100) wafer. Undesired PR residue was removed with O_2 plasma in a reactive ion etching (RIE) chamber. An 8-nm layer of Cr was deposited before lifting off the PR posts with Microposit Remover 1165. RIE was then used to etch ≈200-nm deep holes into the Si wafer and then a 100-nm thin Au film was deposited. The Cr layer was removed via wet etching (Transene Cr Etchant), and the Au film was floated from the Si substrate onto a fused silica substrate. A 50-nm layer of Al was deposited via electron beam deposition before removing the Au film with transparent tape.

Linear Optical Property Measurements: White light transmission spectra were collected from $\theta = -5°$ to 60° at 0.2° increments. The transmitted light was coupled into a bundled optical fiber connected to a Princeton Instruments Acton SP2500 spectrometer with a PIXIS:400 CCD detector. An oil superstrate (refractive index $n = 1.45$) surrounded the NP lattice and was used to match the index of the fused silica ($n = 1.45$) substrate to form high-quality SLR modes. A background dispersion diagram for each polarization was collected with identical parameters to the sample measurements but with clean fused silica as the substrate.

Lasing Measurements: For each lasing measurement, a drop of the dye solution in DMSO was sandwiched between the lattice and a glass ($n = 1.52$) coverslip. A 100-fs pulsed Ti:sapphire laser with a repetition rate of 1 kHz and an optical parameter amplifier (TOPAS Prime, Light Conversion) were used to pump the different dye solutions at a 60° angle of incidence (450 nm for C540A; 534 nm for R6G and LDS821; 665 nm for LD700). The angle-resolved emission was collected with an NA = 0.95 objective and measured with a Princeton Instruments Acton SP2500 spectrometer and a PIXIS:400 CCD detector. A white light transmission measurement of a 500 grooves/mm grating was used to correct for lens distortion.

Supporting Information

Supporting Information is available from the Wiley Online Library or from the author.

Acknowledgements

This work was supported by CMMI-2028773 (in-plane moiré lattice model; F.M.F., T.W.O), the Vannevar Bush Faculty Fellowship from the U.S. Department of Defense (DOD N00014-17-1-3023, F.F.F., T.W.O.), and in part through the computational resources and staff contributions provided for the Quest high performance computing facility at Northwestern University which is jointly supported by the Office of the Provost, the Office for Research, and Northwestern University Information Technology. This work made use of the NUFAB facility of Northwestern University's NUANCE Center, which has received support from the SHyNE Resource (NSF ECCS-2025633), the IIN, and Northwestern's MRSEC program (NSF DMR-1720139). The authors would also like to thank Dr. Thaddeus Reese for his 3D models in Blender.

Conflict of Interest

The authors declare no conflict of interest.

Author Contributions

F.M.F and T.W.O conceived the idea and fabrication method for in-plane incommensurate moiré lattices. F.M.F carried out all fabrication, calculations, and linear optical measurements. F.M.F and F.F.F. carried out the lasing measurements. F.M.F analyzed the data. F.M.F and T.W.O wrote the manuscript. All authors commented on and revised the manuscript.

Data Availability Statement

The data that support the findings of this study are available from the corresponding author upon reasonable request.

Keywords

high rotational symmetry lattices, incommensurate, moiré, nanolasing, photonics, quasiperiodic, surface plasmons

Received: March 22, 2024
Revised: June 7, 2024
Published online:

[1] Y. Cao, V. Fatemi, S. Fang, K. Watanabe, T. Taniguchi, E. Kaxiras, P. Jarillo-Herrero, *Nature*. **2018**, *556*, 43.
[2] X. Wang, C. Xiao, H. Park, J. Zhu, C. Wang, T. Taniguchi, K. Watanabe, J. Yan, D. Xiao, D. R. Gamelin, W. Yao, X. Xu, *Nature*. **2022**, *604*, 468.
[3] J. Gou, L. Kong, X. He, Y. L. Huang, J. Sun, S. Meng, K. Wu, L. Chen, A. T. S. Wee, *Sci. Adv.* **2020**, *6*, eaba2773.
[4] S. Kezilebieke, V. Vaňo, M. N. Huda, M. Aapro, S. C. Ganguli, P. Liljeroth, J. L. Lado, *Nano Lett.* **2022**, *22*, 328.
[5] Y. Cao, V. Fatemi, A. Demir, S. Fang, S. L. Tomarken, J. Y. Luo, J. D. Sanchez-Yamagishi, K. Watanabe, T. Taniguchi, E. Kaxiras, R. C. Ashoori, P. Jarillo-Herrero, *Nature*. **2018**, *556*, 80.
[6] S. M. Lubin, W. Zhou, A. J. Hryn, M. D. Huntington, T. W. Odom, *Nano Lett.* **2012**, *12*, 4948.
[7] J. Daintith, *A Dictionary of Physics*, Oxford University Press, Oxford **2009**.
[8] O. Aftenieva, M. Schnepf, B. Mehlhorn, T. A. F. König, *Adv. Opt. Mater.* **2021**, *9*, 2001280.
[9] J. Guan, J. Hu, Y. Wang, M. J. H. Tan, G. C. Schatz, T. W. Odom, *Nat. Nanotechnol.* **2023**, *18*, 514.
[10] S. M. Lubin, A. J. Hryn, M. D. Huntington, C. J. Engel, T. W. Odom, *ACS Nano*. **2013**, *7*, 11035.
[11] X.-R. Mao, Z.-K. Shao, H.-Y. Luan, S.-L. Wang, R.-M. Ma, *Nat. Nanotechnol.* **2021**, *16*, 1099.
[12] H.-Y. Luan, Y.-H. Ouyang, Z.-W. Zhao, W.-Z. Mao, R.-M. Ma, *Nature*. **2023**, *624*, 282.
[13] S. Zou, N. Janel, G. C. Schatz, *J. Chem. Phys.* **2004**, *120*, 10871.
[14] K. L. Kelly, E. Coronado, L. L. Zhao, G. C. Schatz, *J. Phys. Chem. B.* **2003**, *107*, 668.
[15] D. Wang, A. Yang, A. J. Hryn, G. C. Schatz, T. W. Odom, *ACS Photon.* **2015**, *2*, 1789.
[16] S. R. K. Rodriguez, M. C. Schaafsma, A. Berrier, J. Gómez Rivas, *Phys. B.* **2012**, *407*, 4081.
[17] Q. Le-Van, E. Zoethout, E.-J. Geluk, M. Ramezani, M. Berghuis, J. Gómez Rivas, *Adv. Opt. Mater.* **2019**, *7*, 1801451.
[18] S. Deng, R. Li, J.-E. Park, J. Guan, P. Choo, J. Hu, P. J. M. Smeets, T. W. Odom, *Proc. Natl. Acad. Sci.* **2020**, *117*, 23380.
[19] M. S. Bin-Alam, O. Reshef, Y. Mamchur, M. Z. Alam, G. Carlow, J. Upham, B. T. Sullivan, J.-M. Ménard, M. J. Huttunen, R. W. Boyd, K. Dolgaleva, *Nat. Commun.* **2021**, *12*, 974.
[20] H. Walser, *Zentralblatt für Didaktik der Mathemat.* **2000**, *32*, 32.
[21] R. Bistritzer, A. H. MacDonald, *Proc. Natl. Acad. Sci.* **2011**, *108*, 12233.
[22] J. M. Winkler, M. J. Ruckriegel, H. Rojo, R. C. Keitel, E. De Leo, F. T. Rabouw, D. J. Norris, *ACS Nano*. **2020**, *14*, 5223.
[23] A. Fernandez-Bravo, D. Wang, E. S. Barnard, A. Teitelboim, C. Tajon, J. Guan, G. C. Schatz, B. E. Cohen, E. M. Chan, P. J. Schuck, T. W. Odom, *Nat. Mater.* **2019**, *18*, 1172.
[24] K. S. Daskalakis, A. I. Väkeväinen, J.-P. Martikainen, T. K. Hakala, P. Törmä, *Nano Lett.* **2018**, *18*, 2658.
[25] A. H. Schokker, A. F. Koenderink, *Phys. Rev. B.* **2014**, *90*, 155452.
[26] W. Zhou, M. Dridi, J. Y. Suh, C. H. Kim, D. T. Co, M. R. Wasielewski, G. C. Schatz, T. W. Odom, *Nat. Nanotechnol.* **2013**, *8*, 506.
[27] R. Guo, M. Nečada, T. K. Hakala, A. I. Väkeväinen, P. Törmä, *Phys. Rev. Lett.* **2019**, *122*, 013901.
[28] X. G. Juarez, R. Li, J. Guan, T. Reese, R. D. Schaller, T. W. Odom, *ACS Photonics*. **2022**, *9*, 52.
[29] J. Guan, M. R. Bourgeois, R. Li, J. Hu, R. D. Schaller, G. C. Schatz, T. W. Odom, *ACS Nano*. **2021**, *15*, 5567.
[30] M. P. Knudson, R. Li, D. Wang, W. Wang, R. D. Schaller, T. W. Odom, *ACS Nano*. **2019**, *13*, 7435.
[31] J. Guan, R. Li, X. G. Juarez, A. D. Sample, Y. Wang, G. C. Schatz, T. W. Odom, *Adv. Mater.* **2023**, *35*, 2103262.
[32] F. Freire-Fernández, T. Reese, D. Rhee, J. Guan, R. Li, R. D. Schaller, G. C. Schatz, T. W. Odom, *ACS Nano*. **2023**, *17*, 21905.
[33] A. H. Schokker, A. F. Koenderink, *Optica*. **2016**, *3*, 686.
[34] D. Wang, A. Yang, W. Wang, Y. Hua, R. D. Schaller, G. C. Schatz, T. W. Odom, *Nat. Nanotechnol.* **2017**, *12*, 889.
[35] K. Guo, S. Kasture, A. F. Koenderink, *OSA Continuum*. **2019**, *2*, 1982.
[36] I. Goldberg, N. Annavarapu, S. Leitner, K. Elkhouly, F. Han, N. Verellen, T. Kuna, W. Qiu, C. Rolin, J. Genoe, R. Gehlhaar, P. Heremans, *ACS Photonics*. **2023**, *10*, 1591.
[37] S. I. Azzam, K. Chaudhuri, A. Lagutchev, Z. Jacob, Y. L. Kim, V. M. Shalaev, A. Boltasseva, A. V. Kildishev, *Laser Photonics Rev.* **2021**, *15*, 2000411.
[38] Y. Wu, S. Addamane, J. L. Reno, B. S. Williams, *Appl. Phys. Lett.* **2021**, *119*, 111103.
[39] R. Heilmann, K. Arjas, T. K. Hakala, T. Päivi, *ACS Photonics*. **2023**, *10*, 3955.
[40] E. M. Hicks, S. Zou, G. C. Schatz, K. G. Spears, R. P. Van Duyne, L. Gunnarsson, T. Rindzevicius, B. Kasemo, M. Käll, *Nano Lett.* **2005**, *5*, 1065.
[41] M. H. Lee, M. D. Huntington, W. Zhou, J.-C. Yang, T. W. Odom, *Nano Lett.* **2011**, *11*, 311.
[42] J. Henzie, M. H. Lee, T. W. Odom, *Nat. Nanotechnol.* **2007**, *2*, 549.